Adaptive Gaussian Weighted Laplace Prior Regularization Enables Accurate Morphological Reconstruction in Fluorescence Molecular Tomography

Hui Meng, Kun Wang, Yuan Gao, Yushen Jin, Xibo Ma, and Jie Tian, *Fellow, IEEE*

***Abstract*— Fluorescence molecular tomography (FMT), as a powerful imaging technique in preclinical research, can offer the three-dimensional distribution of biomarkers by detecting the fluorescently labelled probe noninvasively. However, because of the light scattering effect and the ill-pose of inverse problem, it is challenging to develop an efficient reconstruction method, which can provide accurate location and morphology of the fluorescence distribution. In this research, we proposed a novel adaptive Gaussian weighted Laplace prior (AGWLP) regularization method, which assumed the variance of fluorescence intensity between any two voxels had a non-linear correlation with their Gaussian distance. It utilized an adaptive Gaussian kernel parameter strategy to achieve accurate morphological reconstructions in FMT. To evaluate the performance of the AGWLP method, we conducted numerical simulation and in vivo experiments. The results were compared with fast iterative shrinkage (FIS) thresholding method, split Bregman-resolved TV (SBRTV) regularization method, and Gaussian weighted Laplace prior (GWLP) regularization method. We validated *in vivo* imaging results against planar fluorescence images of frozen sections. The results demonstrated that the AGWLP method achieved superior performance in both location and shape recovery of fluorescence distribution. This enabled FMT more suitable and practical for *in vivo* visualization of biomarkers.**

***Index Terms*— Fluorescence tomography, multi-modality fusion, brain.**

I. Introduction

FLUORESCENCE molecular imaging (FMI) can noninvasively image biomarkers by detecting the distribution of targeted fluorescence probes in biological tissue [1]–[3]. However, due to the absorption and scattering effect of photon propagation, FMI only provides the qualitative planar photon distribution information on the surface of an imaging object, which does not reflect the 3D spatial distribution of fluorescence probes. This limits the application of FMI for studies on the spatial heterogeneity in tumors. Therefore, continued efforts have been devoted to developing fluorescence molecular tomography (FMT), which is supposed to restore the 3D distribution of interior fluorescence probes [4], [5]. FMT holds great potential for the research on tumor heterogeneity, because there is still not an ideal tool for *in vivo* 3D visualization of special biomarkers [6], [7].

To improve the quality of FMT reconstruction, several methods have been proposed. One effective strategy is utilizing the spatial distribution of different biological tissues, which can be segmented from computed tomography (CT) and magnetic resonance imaging (MRI), as a prior information to construct the photon propagation model [8], [9]. Furthermore, optimization methods with different regularizations were also used to alleviate the ill-posed problem in FMT reconstruction. One of the major methods is adopting assumption that the fluorescence source is sparse compared with the entire reconstruction region, so either sparse regularization terms (L_0, L_1, L_p $(0<p<1)$, etc.) [10]–[13] or greedy strategies [14], [15] were able to be employed. Besides, total variation regularization methods [16]–[18] have been proposed to preserve sharp transitions in FMT reconstruction. Tikhonov regularization with different regularization matrices have also been widely used in reconstruction [8], [19]. Although most of these methods continuously improved the location accuracy of fluorescence sources, there was only few success in the accurate morphological reconstruction of fluorescence distributions.

Manuscript received March 5, 2019; revised April 10, 2019; accepted April 15, 2019. Date of publication April 22, 2019; date of current version November 26, 2019. This work was supported in part by the Ministry of Science and Technology of China under Grant 2017YFA0205200 and Grant 2016YFA0100902, in part by the National Natural Science Foundation of China under Grant 61671449, Grant 81227901, Grant 81471739, and Grant 81527805, and in part by the Chinese Academy of Sciences under Grant GJJSTD20170004, Grant KFJ-STS-ZDTP-059, Grant YJKYYQ20180048, and Grant QYZDJ-SSW-JSC005. *(Hui Meng and Kun Wang contributed equally to this work.) (Corresponding authors: Kun Wang; Jie Tian.)*

H. Meng and Y. Gao are with the CAS Key Laboratory of Molecular Imaging, Institute of Automation, Beijing 100190, China, and also with the School of Artificial Intelligence, University of Chinese Academy of Sciences, Beijing 100080, China (e-mail:menghui2015@ia.ac.cn; gaoyuan2014@ia.ac.cn).

K. Wang, Y. Jin, and X. Ma are with the CAS Key Laboratory of Molecular Imaging, Institute of Automation, Beijing 100190, China, also with the School of Artificial Intelligence, University of Chinese Academy of Sciences, Beijing 100080, China, and also with the Beijing Key Laboratory of Molecular Imaging, Beijing 100190, China (e-mail: kun.wang@ia.ac.cn; yushen.jin@ia.ac.cn; xibo.ma@ia.ac.cn).

J. Tian is with the CAS Key Laboratory of Molecular Imaging, Institute of Automation, Beijing 100190, China, also with the Beijing Key Laboratory of Molecular Imaging, Beijing 100190, China, and also with the Beijing Advanced Innovation Center for Big Data-Based Precision Medicine, Beihang University, Beijing 100191, China (e-mail: tian@ieee.org).

This article has supplementary downloadable material available at http://ieeexplore.ieee.org, provided by the author.

Color versions of one or more of the figures in this article are available online at http://ieeexplore.ieee.org.

Digital Object Identifier 10.1109/TMI.2019.2912222

In the study of orthotopic glioma morphological FMT reconstruction, several work have been reported that the morphology of fluorescence distribution can be recovered [7], [20]–[22]. The major strategy of these reconstruction methods is adopting the tumor region prior which segmented from the other structural imaging modalities (CT, MRI). Thus, the region of reconstructed fluorescence source is heavily depended on these non-optical imaging modalities, and did not present the specific distribution of biomarker. The distribution of targeted fluorescence probes is not entirely consistent with the real or segmented tumor region [23]–[25], which suggests that such pre-defined prior from imaging segmentation is likely to be improper for obtaining accurate biomarker distribution. Thus, there is a pressing need for a method that can provide accurate morphological reconstruction of the fluorescence source distribution without the segmented tumor region prior. However, existing methods for FMT reconstruction have not obtained satisfactory results [26]. The over-smoothed effect and low contrast-to-noise ratio still influenced the shape recovery in FMT reconstruction. In this study, we proposed an adaptive Gaussian weighted Laplace prior (AGWLP) regularization method to overcome the over-smoothed effect and improve contrast-to-noise ratio. AGWLP method reconstructed the fluorescence source without using the segmented tumor region prior and yet obtained superior morphological reconstruction of fluorescence distribution in glioma.

AGWLP method adopted an emerging assumption that the variance of fluorescence intensity between any two voxels has a non-linear inverse correlation with their Gaussian distance [27]. Based on this assumption, an adaptive Gaussian kernel parameter strategy was designed to adaptively adjust the weight of Gaussian distance of voxels with different fluorescence intensity. This strategy aimed to effectively overcome the problems of over-smooth and low contrast-to-noise ratio in FMT reconstruction, and improve the quality of morphological reconstruction without tumor region prior.

To assess the performance of AGWLP method, simulation and *in vivo* experiments in orthotopic glioma models were implemented. Fast iterative shrinkage (FIS) thresholding method, Split Bregman-resolved TV (SBRTV) regularization method, Gaussian weighted Laplace prior (GWLP) regularization method and kernel method [13], [16], [27], [28] were used for comparisons. The results of AGWLP method showed significant improvement in both localization and shape recovery of the fluorescence distribution.

This paper is organized as follows: Section II introduces the forward and inverse models of FMT reconstruction, the reconstruction algorithm based on AGWLP method, the design of *in vivo* experiments and the evaluation index. Section III presents the results of simulation and *in vivo* experiments. At last, Section IV gives conclusion and discussion of our proposed method.

II. Methodology

A. Photon Propagation Model of Fmt

For steady-state FMT reconstruction, the propagation of light in biological tissue can be modeled by the coupled diffusion equations with Robin-type boundary condition [26], which is defined as:

$$\begin{cases} \nabla \cdot (D_x(\mathrm{r})\nabla\Phi_x(\mathrm{r})) - \mu_{ax}(\mathrm{r})\Phi_x(\mathrm{r}) \\ \quad = -\Theta\delta(r - r_l) & r \in \Omega \\ \nabla \cdot (D_m(\mathrm{r})\nabla\Phi_m(\mathrm{r})) - \mu_{am}(\mathrm{r})\Phi_m(\mathrm{r}) \\ \quad = -\Phi_x(\mathrm{r})\eta\mu_{af}(\mathrm{r}) & r \in \Omega \\ 2D_{x,m}(\mathrm{r})\nabla\Phi_{x,m}(\mathrm{r}) + q\Phi_{x,m}(\mathrm{r}) = 0 & r \in \partial\Omega \\ D_{x,m} = 1/3(\mu_{ax,am} + (1-g)\mu_{sx,sm}) \end{cases} \tag{1}$$

where ∇ denotes the gradient operator, and r is the location vector inside the imaging domain Ω. r_l is the positions of excitation source with the amplitude Θ, which is seated at one transport mean free path beneath the surface of biological tissue. Subscripts x and m are the excitation and emission process, respectively. $\Phi_{x,m}(r)$ denotes the photon flux density (W/mm^2) at position r. $\mu_{ax,am}$ and $\mu_{sx,sm}$ are the absorption coefficients and scattering coefficients in mm^{-1}, respectively. $D_{x,m}$ is the diffusion coefficient, and g denotes the anisotropy parameter. $\eta\mu_{af}(r)$ is the fluorescent source to be reconstructed, where η is the quantum efficiency. q is the optical reflective index.

Based on finite element analysis, (1) can be transformed into the following equation [29]:

$$\Phi = AX \tag{2}$$

where Φ denotes the measured light flux on the object surface, A denotes the system matrix, and X is the distribution of fluorescent sources in biological tissues [30].

B. Inverse Problem of Reconstruction

FMT reconstruction is aimed to solve the inverse problem of (2). Because of the noise in the FMI measurement and the ill-posed problem in system matrix A, unconstrained optimization with Tikhonov regularization strategies are widely utilized to obtain the optimal approximate solution of the fluorescent source distribution X [19]. The unconstrained optimization of FMT reconstruction with Tikhonov regularization is defined as

$$\min E(X) = \frac{1}{2} \parallel AX - \Phi \parallel_2^2 + \lambda \parallel LX \parallel_2^2 \tag{3}$$

where λ is the regularization parameter utilized to control the tradeoff between the regularity term and fidelity term. L-curve analysis was utilized to determine the value of λ in all experiments (Fig. S1 and Fig. S2). L denotes the regularization matrix and it is defined widely as an identity matrix. However, Tikhonov regularization with identity matrix usually causes the over-smoothed effect in FMT reconstructions. Therefore, the anatomical structure and intensity distribution are adopted as the prior information to construct the regularization matrix to alleviate this problem.

C. Reconstruction Based on Adaptive Gaussian Weighted Laplace Prior Regularization

In this section, we proposed a practical AGWLP method, which was inspired by the GWLP method firstly developed for bioluminescence tomography (BLT) [27], to improve the

overall effect of FMT reconstruction. GWLP constructs the regularization matrix L with the Gaussian distance of each couple voxels, and the regularization matrix is given as follows [27]

$$L_G = (l_{i,j})_{N\times N} \tag{4}$$

$$l_{i,j} = \begin{cases} 1 & i = j \\ -\rho_{sk}\exp(\frac{-d_{i,j}^2}{4R^2}) & i, j \in S_t \,\&\, i \neq j \\ 0 & otherwise \end{cases} \tag{5}$$

$$\rho_{sk} = 1/(\sum\nolimits_{\forall i,j\in S_t, i\neq j} \exp(\frac{-d_{i,j}^2}{4R^2})) \tag{6}$$

where each element $l_{i,j}$ in L_G is named as the decay element. S_t denotes the sub-image t, and $d_{i,j}$ is Euclidean distance between voxels i and j. ρ_{sk} is the radial mollifier. R is the radius of the Gaussian kernel, which is a constant for all voxels in the GWLP method. Although GWLP successfully provided morphological information of glioma in BLT reconstructions, the drawbacks of over-smooth and low contrast-to-noise ratio exhibited in FMT reconstructions. To overcome these problems, here we proposed the AGWLP method utilizing an adaptive rather than a fixed Gaussian Kernel parameter designed in GWLP. AGWLP divided the targeting voxels into three groups, the high-intensity group Ω_h, the middle-intensity group Ω_m, and the low-intensity group Ω_l.

$$\Omega_h = \left\{k | X_k^n \geq \theta_h X_{\max}^n, 1 \leq k \leq N\right\} \tag{7}$$

$$\Omega_m = \left\{k | \theta_l X_{\max}^n \leq X_k^n \leq \theta_h X_{\max}^n, 1 \leq \mathrm{k} \leq N\right\} \tag{8}$$

$$\Omega_l = \left\{k | X_k^n \leq \theta_l X_{\max}^n, 1 \leq k \leq N\right\} \tag{9}$$

where X_k^n and X_{max}^ndenote the intensity of the k-th voxel and the maximum intensity of voxels calculated in the n-th iteration, respectively. θ_h and θ_l are thresholds used to divide voxels into the three groups. Because large Gaussian kernel parameters tend to decrease the intensity variance of adjacent voxels and cause the smoothing effect [31], we assigned a large Gaussian kernel parameter R_L to voxels belonging to Ω_h and Ω_l. Therefore, the high-intensity region can be better defined, as well as the background signals can be weakened. Furthermore, a small Gaussian kernel parameter R_S was assigned to voxels in Ω_m to preserve the boundary information of the fluorescence source. Based on this strategy, the regularization matrix L_{AG} is defined as follows

$$L_{AG} = (l_{i,j})_{N\times N} \tag{10}$$

$$l_{i,j} = \begin{cases} 1 & i = j \\ -\rho_{sk}\exp(\dfrac{-d_{i,j}^2}{4R_L^2}) & i, j \in S_t \;\&\; i \neq j \;\&\; i \in (\Omega_h \cup \Omega_l) \\ -\rho_{sk}\exp(\dfrac{-d_{i,j}^2}{4R_S^2}) & i, j \in S_t \;\&\; i \neq j \;\&\; i \in \Omega_m \\ 0 & otherwise \end{cases} \tag{11}$$

$$\rho_{sk} = 1/(\sum\nolimits_{\forall i,j\in S_t, i\neq j. i\in(\Omega_h\cup\Omega_l)} \exp(\frac{-d_{i,j}^2}{4R_L^2}) + \sum\nolimits_{\forall i,j\in S_t, i\neq j. i\in\Omega_m} \exp(\frac{-d_{i,j}^2}{4R_S^2})) \tag{12}$$

In this study, the initial parameters were set as $R_L = R_S$, so the first iteration solution is equal to (4). The parameters θ_h and θ_l were set as 0.95 and 0.1, respectively. In dual-source reconstruction, R_S and R_L were chosed to be 1 and 6, respectively. In morphological reconstruction, we used $R_s = 0.4$ and $R_L = 20$ to obtain accurate FMT reconstruction. The comparisons of different parameters R and θ are provided in the Supplementary Material Section S.I.B and S.I.C, respectively. Supplementary materials are available in the supplementary files / multimedia tab.

Fletcher-Reeves conjugate gradient (CG) method [32] was introduced to solve the inverse problem of (3). Thus, the AGWLP method can be summarized in Algorithm 1.

Algorithm 1 AGWLP Method

Preprocess

1: Mapping the fluorescence images to the high-resolution CT data.

2: Segmenting CT data into muscle, skull, and brain, then labeling them as sub-images.

Step 1: Calculating the system matrix A by (1)

Step 2: Initializing the regularization matrix by (4) and constructing the optimization function by (3).

Step 3: Using CG method to solve the inverse problem. In each loop, the regularization matrix are updated by (10), and the calculated intensities of voxels are corrected based on the non-negativity prior.

D. In Vivo Experiment

Male BALB/c nude mice were obtained from the Beijing Vital River Laboratory Animal Technology Co. Ltd. All animal experiments were implemented under the guideline approved by the Institutional Animal Care and Use Committee at Peking University. A newly designed fluorescence probe, Tf-IRDye800, was employed for *in vivo* imaging. To prepare it, 0.34 mg NH2-PEG-COOH (Innochem) and 0.1 mg IRDye800-NHS (LI-COR Bioscience) were dissolved in 4 mL phosphate-buffered saline (PBS, pH 7.4) and stirred for 1 hour. Then we added 6.6 mg transferrin (Sigma-Aldrich), 0.16mg 1-(3-Dimethylaminopropyl)-3-ethylcarbodiimide hydrochloride (Innochem), and 0.09mg N-Hydroxy succinimide (Innochem) to the mixture, and the mixture was incubated at the room temperature for 24 hours under constant shaking at 500 rpm. Finally, the probe was purified by ultrafiltration through a membrane (cutoff = 50 kDa) and redissolved in 5 mL PBS.

All animal experiments were implemented under isoflurane gas anaesthesia (500 mL/min, Matrx VMR Small Animal Anesthesia Machine, Matrx, USA), and all efforts were made to alleviate the pain of the mice. To build the orthotopic glioma models, 5×10^5 U-87 MG cells in 6 μl PBS were injected into the brain of each mouse (0.5 mm anterior and 2 mm right to the bregma at a depth of 2.5 mm). After 7 days, the tumor-bearing mice were injected with 200 μL Tf-IRDye800 through the tail vein. After 6 hours, the surface fluorescence images and CT data were acquired utilizing a

TABLE I
OPTICAL PARAMETERS USED IN NUMERICAL SIMULATION AND IN VIVO EXPERIMENTS

Organ	$\mu_{ax}(mm^{-1})$	$\mu_{sx}(mm^{-1})$	$\mu_{am}(mm^{-1})$	$\mu_{sm}(mm^{-1})$
Muscle	0.0474	0.3122	0.0287	0.2427
Skull	0.0326	2.1140	0.0197	1.8541
Brain	0.0183	1.3784	0.0167	1.2156

pentamodal imaging system designed by our group [33], [34] and the MRI scan (1.5t, M3TM, Aspect Imaging, Israel) was implemented subsequently.

During the optical image acquisition, we used a 750 nm continuous wave semiconductor laser with the output power of 450 mW to provide the excitation illumination. We collected fluorescence images using an electron multiplying charge coupled device (EMCCD) camera (iXonEM+888, ANDOR, UK) with 4 × 4 binning and 0.5 s exposure. A 25 nm band-pass filter centered at 820 nm was used to capture the emission light and limit the background noise. Besides the collection of optical images, we acquired CT data to provide structural prior information. Major corresponding organs like skull, brain, and muscle were segmented from the CT data, and their optical properties [35], [36] were shown in Table. I. T2-weighted MR images were collected with the following parameters: TR 6000 ms, TE 50 ms, slice thickness 0.8 mm, and slice spacing 0.1 mm [27].

After the *in vivo* triple-modality imaging, frozen sections of each mouse head were collected utilizing freezing microtome (CM1950, Leica, Germany). Meanwhile, the *ex vivo* near infrared fluorescence (NIRF) images of frozen sections were acquired using a Live Cell Imaging System (AF6000 Modular System, Leica, Germany) attached with a sensitive CCD camera (Princeton Instruments, ProEM 1024B). Lastly, these specimen were stained by hematoxylin and eosin (H&E) for verifying the actual tumor area.

E. The Evaluation Index

To quantitative evaluate the accuracy of FMT reconstruction in both source location and shape recovery, location error (LE), contrast-to-noise ratio (CNR) and Dice index were used as the quantitative indexes. LE measures the distance variation between the centers of the actual region and the reconstructed region. LE is defined as

$$LE = \| L_a - L_r \|_2 \tag{13}$$

where L_a and L_r denote the center coordinates of the actual region and the reconstructed region, respectively. $||\cdot||_2$ represents the operator of Euclidean distance.

CNR indicates the detectability of fluorescent sources within reconstructed images from the background [37]. The higher the CNR value, the easier it is to distinguish the source from the background. The definition of CNR is presented as follows:

$$CNR = \frac{\mu_{ROI} - \mu_{ROB}}{\sqrt{\omega_{ROI}\sigma^2_{ROI} - \omega_{ROB}\sigma^2_{ROB}}} \tag{14}$$

where μ_{ROI} and μ_{ROB} are the mean intensity values of the region of interest (ROI) and region of background (ROB),

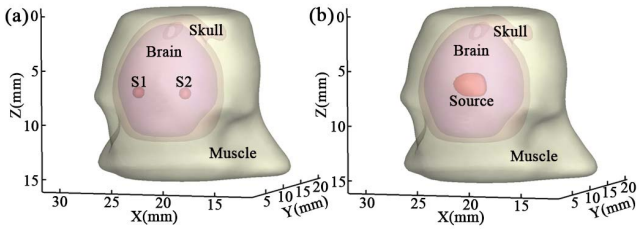

Fig. 1. The views of simulation models with the dual-source (a) and the chestnut shaped source (b).

σ^2_{ROI} and σ^2_{ROB} are the respective variances. ω_{ROI} and ω_{ROB} are the ratios of ROI and ROB relative to the whole region. Furthermore, we adopted the Dice index to assess the quality of morphological reconstructions.

$$Dice = \frac{2|X \cap Y|}{|X| + |Y|} \tag{15}$$

where X and Y represent the point sets of the reconstructed region and the actual region, respectively. Higher Dice index reveals a better similarity of the two regions in both location and morphology.

III. RESULTS

In this section, we evaluated the performance of AGWLP using numerical simulation studies and *in vivo* probe distribution studies. This section is organized as follows: first, dual fluorescence source experiments were presented to verify the location accuracy and robustness (Fig. 1(a)). Second, the morphological reconstruction accuracy was evaluated in the chestnut shaped source reconstruction (Fig. 1(b)). Last, *in vivo* reconstructions of the fluorescent probe distribution in orthotopic glioma mouse models were demonstrated to prove the practicability of AGWLP.

A. Dual-Source Reconstruction

The dual-source simulation studies were firstly implemented to evaluate the location accuracy and robustness of AGWLP. A mouse CT atlas [27] was utilized to construct a heterogeneous phantom, and two spherical sources, S1 and S2, were set inside the brain, as shown in Fig. 1(a). The centers of S1 and S2 are (23.5, 4.4, 7.0) mm and (18.9, 4.4, 7.0) mm. The radius and depth of sources are 0.56 mm and 2 mm, respectively. In the forward process, the simulation model was divided into 13150 nodes and 69826 tetrahedral elements. To avoid the inverse crime, elements used in the inverse process were different from the forward process, which contained 9726 nodes and 51055 tetrahedrons.

Fig. 2 shows the reconstructed dual fluorescence sources in 3D rendered and 2D axial images using different methods. The 2D axial slices crossing both fluorescent centers (Z = 7 mm) are specially selected for the comparison, and quantifications of LE are listed in Table. II. These comparisons were performed with zero (Fig. 2(a)) and 15% (Fig. 2(b)) Gaussian noise in surface flux signals, respectively, and results revealed good source location tracing ability of all methods besides SBRTV. Comparing with other methods, SBRTV failed to

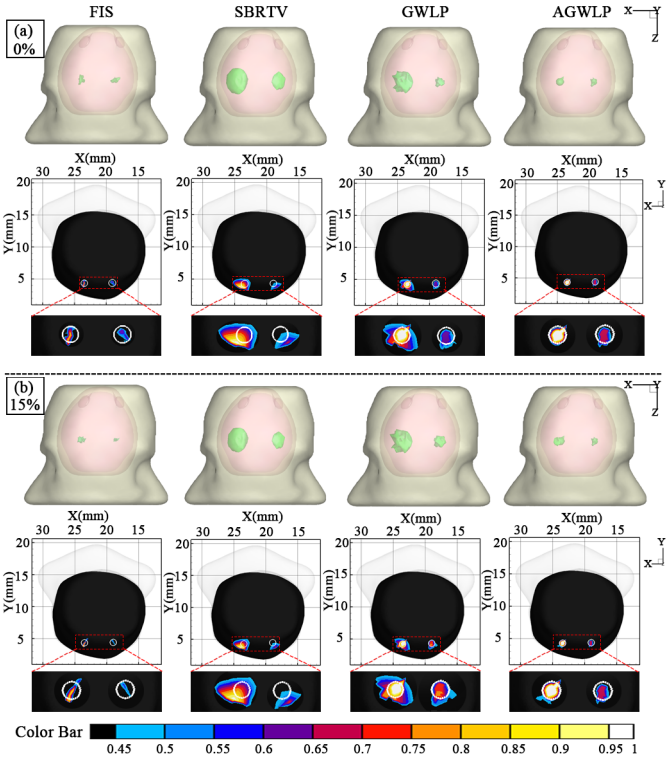

Fig. 2. FMT reconstruction results of dual fluorescent sources using different approaches. (a) 0% and (b) 15% Gaussian noise was added in simulations. Both 3D rendering images and 2D axial slices are presented for comparisons. White circles in 2D axial slices indicate the ground truth of the fluorescent sources.

TABLE II
QUANTITATIVE RESULTS OF LE IN THE DUAL-SOURCE SIMULATION

Method	Noise intensities	
	0%	15%
FIS	S1: 0.002 mm S2: 0.009 mm	S1: 0.015 mm S2: 0.015 mm
SBRTV	S1: 0.068 mm S2: 0.313 mm	S1: 0.067 mm S2: 0.427 mm
GWLP	S1: 0.029 mm S2: 0.039 mm	S1: 0.029 mm S2: 0.064 mm
AGWLP	S1: 0.007 mm S2: 0.018 mm	S1: 0.020 mm S2: 0.018 mm

trace the correct barycenter of S2 in both noise levels. For FIS, GWLP, and AGWLP, even though the extra 15% noise indeed increased their biases, all corresponding LEs were still smaller than 0.1 mm in general (Table. II), which proved they all achieved high accuracy in source location reconstructions.

However, regarding to the morphological reconstruction, FIS provided over-sparse results, whereas GWLP provided over-inflated results within the same scale range. On the contrary, AGWLP demonstrated a much better spatial overlap between reconstructed and true sources regardless the noise level (Fig. 2). These comparisons suggested the AGWLP method had superior morphological reconstruction capability.

Besides these results, the comparisons of AGWLP and kernel method in dual-source reconstruction were demonstrated in the Supplementary Material Section S.II.A. Supplementary materials are available in the supplementary files / multimedia tab.

B. Chestnut Shaped Source Reconstruction

Different from using regular spherical sources, we adopted a chestnut shaped source in the simulation model to further compare their performances for rebuilding the source morphology (Fig. 1(b)). The center of the chestnut shaped source is (20.8, 3.9, 6.1) mm. The axis length along x-axis, y-axis and z-axis is 3.2 mm, 1.6 mm, and 2.3 mm, respectively. The depth of the source is 1.7 mm. In the forward process, the simulation model was meshed to 13202 nodes and 70266 tetrahedral elements. In the inverse process, the meshed simulation model contained 9726 nodes and 51055 tetrahedrons.

Fig. 3 presents the reconstruction results of four methods, and Table. III lists their quantifications of LE, Dice, and CNR, respectively. Different from the previous simulation experiment, FIS, instead of SBRTV, showed the largest LE (0.51 mm), indicating the worst location tracing. GWLP and AGWLP offered much smaller spatial biases (both LE $<$ 0.1 mm) than FIS and SBRTV did (Table. III). Regarding to the source morphology, FIS still offered an over-sparse reconstruction, which was consistent with the dual-source simulation. SBRTV and GWLP achieved much better morphological reconstructions (Fig. 3(a)), as the Dice was increased from 0.18 to 0.50 and 0.44, respectively. It is still AGWLP that provided the most accurate reconstruction of the source morphology, with Dice of 0.79.

Besides the most accurate reconstruction of the source location and morphology, AGWLP also achieved the best recurrence of the source intensity. Comparing with FIS, SBRTV, and GWLP, AGWLP provided remarkably higher fluorescent intensity within the reconstructed source volume (Fig. 3(a)). The comparison of intensity profiles between each method revealed that AGWLP showed the highest similarity to the true reference in transverse, coronal, and sagittal views (Fig. 3(b-d)). The over-smoothed effect appeared in SBRTV and GWLP were effectively suppressed. This was further quantified by CNR. The CNR obtained by AGWLP was 12.87, which was about 5.4 times that of FIS, about 1.5 times that of SBRTV, as well as about 2.8 times that of GWLP (Table. III). All these simulated results demonstrated a solid validation that AGWLP achieved the most accurate fluorescence source reconstruction in location, morphology, and intensity.

The different performance of AGWLP and kernel method were provided in the Supplementary Material Section S.II.B. Supplementary materials are available in the supplementary files / multimedia tab.

C. In Vivo Experiment

To assess the practicability of the AGWLP method for small animal studies, we conducted the *in vivo* FMT in three orthotopic glioma mouse models. Through the maximum mutual information registration [38], the reconstructed FMT images given by four methods were merged with the MRI data according to the boundary of the mouse brain [27].

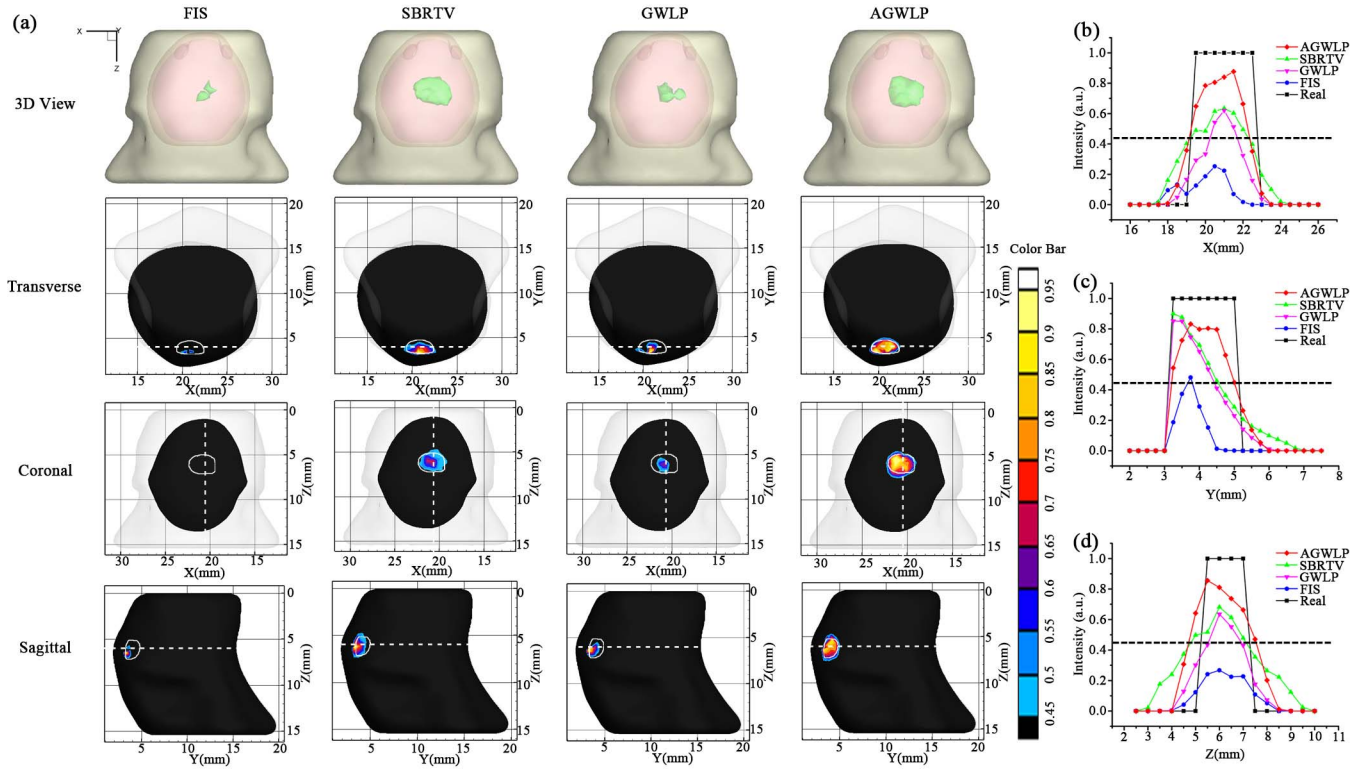

Fig. 3. FMT reconstructions of the chestnut shaped source using different methods. (a) The 3D rendering, transverse view, coronal view, and sagittal view of the source given by FIS, SBRTV, GWLP, and AGWLP, respectively. The intensity distribution of the reconstructed results along the x-axis (b), y-axis (c), and z-axis (d) in comparison with the actual fluorescence source profile. White dotted lines in (a) indicate the location of the intensity profile. White circles in (a) present the ground truth of fluorescent sources. Black dotted lines in (b-d) indicate the threshold of 0.45.

TABLE III
QUANTITATIVE RESULTS FOR FOUR FMT RECONSTRUCTION METHODS IN THE CHESTNUT SHAPED SOURCE SIMULATION

Method	Location error (mm)	Dice	CNR
FIS	0.51	0.18	2.40
SBRTV	0.17	0.50	8.82
GWLP	0.09	0.44	4.65
AGWLP	0.01	0.79	12.87

Fig. 4(a) presents the 3D rendering of the CT data with the MRI-segmented tumor region (blue) and AGWLP reconstructed fluorescence source region (red) for each tumor-bearing mouse. Apparently, these two regions overlapped, but did not completely coincide. Moreover, the four FMT reconstruction methods also showed very different performances in this *in vivo* experiment. FIS still provided over-sparse reconstructions in all three mice, which was consistent with simulation experiments (Fig. 4(b)). The fluorescence sources given by SBRTV and GWLP were relatively similar. They both partially solved the over-sparse problem in FIS. However, their reconstructed areas were still smaller than the corresponding tumor regions defined by MRI in all three mice, and they were also obviously smaller than the fluorescent areas defined by the *ex vivo* NIRF imaging of frozen sections (Fig. 4(b) and (c)). The major reason causing such "shrunken" reconstruction was the over-smooth effect. The high signal region (coded in yellow and red) only appeared in the small central area in the reconstructed source, but it gradually faded from the center to the periphery (coded in purple and blue). Even though we could adjust the color scale to artificially extend its source volume, the overall CNR was always small. This phenomenon was especially stronger in the deeper region of the brain. Comparing with the *ex vivo* references, both SBRTV and GWLP failed to reconstruct fluorescence source in deeper tissues, which compromised the morphological information of the probe distribution.

AGWLP successfully overcame the over-smooth problem in each mouse. Comparing with SBRTV and GWLP, it offered a much larger area of high signal intensities (Fig. 4(b)). The purple and blue area in the source periphery was narrower, giving a sharp boundary of the reconstructed source. This remarkably improved the overall CNR of reconstructed sources. More importantly, it obtained more fluorescent information from the deeper tissue in each mouse, which was also closer to the real probe distribution visualized in the NIRF images of frozen sections (Fig. 4(c)).

To analyze the results quantitatively, Dice index between the reconstructed results of each method and the *ex vivo* NIRF images of frozen sections was calculated and listed in Table. IV. The average $\pm$ standard deviation (SD) of the Dice index given by AGWLP was 0.86 ± 0.04, which was significantly higher than that of the other methods (improvements in percentage: FIS: 323.0%, $P < 0.001$; SBRTV: 48.3%, $P < 0.05$; GWLP: 23.4%, $P < 0.05$). These results further revealed the superior performance of AGWLP in obtaining the morphology of the *in vivo* fluorescence probe distribution in orthotopic glioma mouse models.

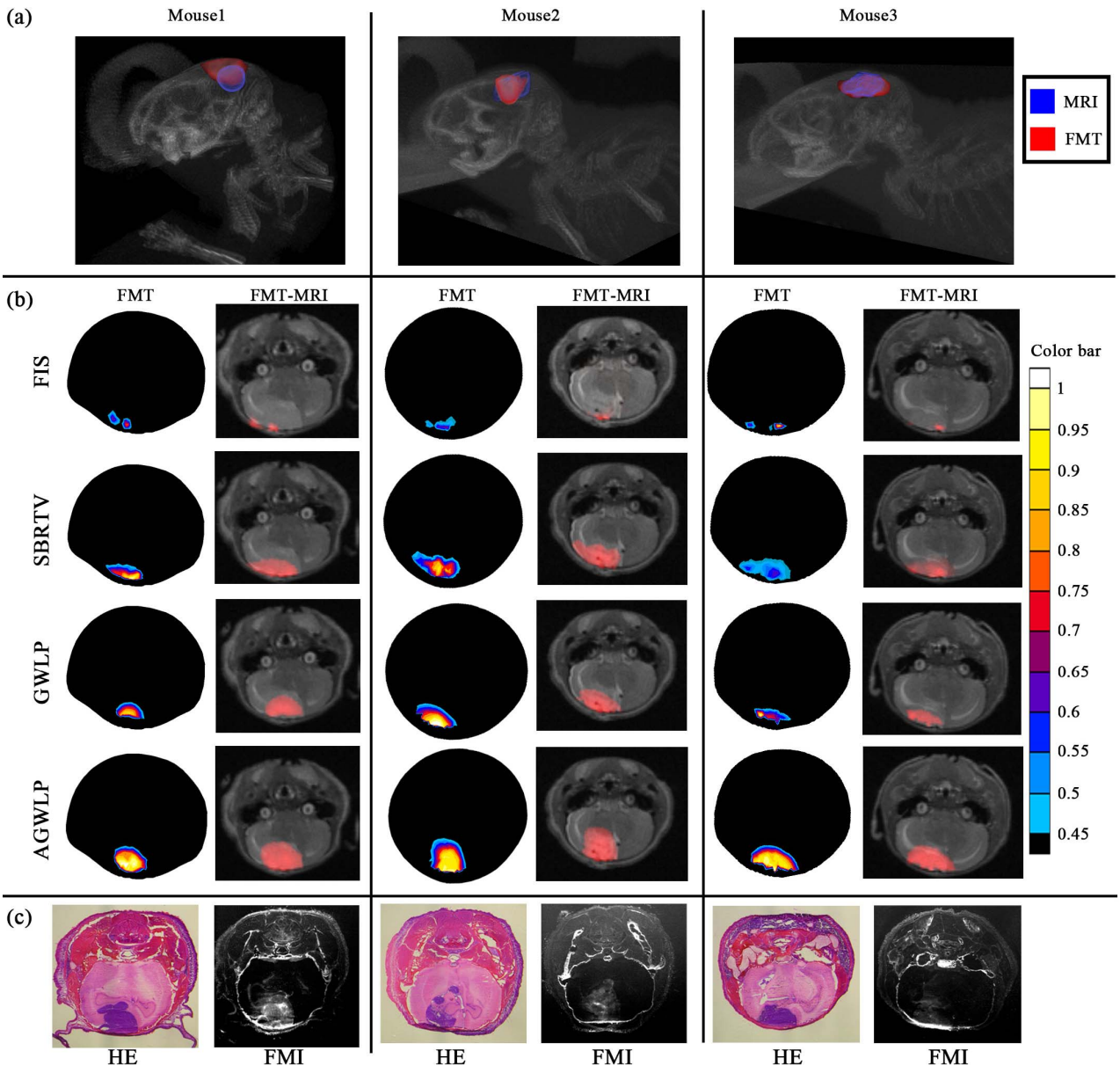

Fig. 4. *In vivo* FMT of three orthotopic glioma bearing mouse models. (a) 3D rendering of the triple-modality imaging. The MRI segmented tumor (blue region) and FMT reconstructed fluorescence source (red region) are fused in the CT data volume. (b) Comparison of reconstructed fluorescence sources using four methods in the same axial slice of FMT and FMT-MRI. (c) H&E stained cryoslicing images and their corresponding near infrared fluorescence images of frozen sections.

TABLE IV
QUANTITATIVE RESULTS OF DICE FOR FOUR FMT RECONSTRUCTION METHODS IN *in vivo* EXPERIMENTS

Method	Mouse 1	Mouse 2	Mouse 3	Average ± SD
FIS	0.19	0.26	0.16	0.20 ± 0.05
SBRTV	0.50	0.65	0.59	0.58 ± 0.08
GWLP	0.74	0.66	0.69	0.70 ± 0.04
AGWLP	0.87	0.89	0.82	0.86 ± 0.04

SD: Standard Deviation

The reconstruction results of five orthotopic glioma mouse models using FIS thresholding method, SBRTV regularization method, GWLP regularization method, kernel method and AGWLP method were presented in the Supplementary Material Section S.II.C. Supplementary materials are available in the supplementary files / multimedia tab.

IV. CONCLUSION AND DISCUSSION

In this paper, a novel AGWLP strategy was proposed to achieve the morphological FMT reconstruction independent from the tumor region prior segmented from anatomical imaging modalities. Based on the assumption that the variance of fluorescence intensity between any two voxels has a non-linear correlation with the Gaussian distance between them [27], AGWLP utilized an adaptive Gaussian kernel parameter strategy to dynamically adjust the Gaussian weight depending on the fluorescence intensity of reconstruction. With the help of this strategy, AGWLP overcame the over-smoothing problem and improved the contrast-to-noise ratio of reconstructed sources.

To validate its performance, we conducted the dual-source simulation and chestnut shaped source simulation experiments.

FIS, SBRTV and GWLP were employed for qualitative and quantitative comparisons. All results revealed that AGWLP achieved the best fluorescence source reconstruction in both 3D localization and morphology recovery. To further assess the practicability of AGWLP, we administrated the transferrin targeting NIRF probes in three orthotopic glioma mouse models, and acquired FMI-CT-MRI triple-modality imaging data. The *ex vivo* H&E stained cryoslicing images and NIRF images of frozen cryo-sections were also acquired as gold standards to verify the performance of AGWLP. Consistent with our simulation experiments, AGWLP still achieved the best reconstruction of the *in vivo* probe distribution by minimizing the over-smooth effect and improving CNR. The average Dice index given by AGWLP reached 0.86, which was significantly higher than that of the other three methods. These results proved that AGWLP successfully achieved the accurate morphological reconstruction of fluorescence sources in tumor-bearing mice.

To our best knowledge, this is the first study that acquired such level of accuracy regarding to the morphological reconstruction of fluorescence distribution in tumor-bearing mouse models with only organ level structural prior rather than the tumor region prior segmented from CT or MRI. This enabled FMT as a more powerful molecular imaging tool for small animal studies in the field of oncology. Our *in vivo* experiment (Fig. 4) vividly demonstrated that there were marked differences between the glioma cell distribution (H&E staining), the fluorescence probe distribution (NIRF images of cryo-sections), as well as the MRI defined glioma distribution. AGWLP based FMT provides a new quantitative approach that can visualize such differences *in vivo* with reliable morphological accuracy, so that the biochemical events at the cellular and molecular level within glioma-bearing mouse models can be further investigated in more details.

The major limitations of AGWLP are that the threshold used to classify the intensity level of voxels and Gaussian kernel parameters were selected based on experience. It is necessary to propose an adaptive parameter selection algorithm to set these parameters objectively. Furthermore, since AGWLP needs to update the regularization matrix based on the calculated results during the iteration, it takes about two minutes to accomplish one FMT reconstruction using a personal computer. Besides that, AGWLP was only utilized to reconstruct the fluorescence probe distribution in the brain in this study. Its application and performance in other tumor types or diseases need further investigations, which is also a major work in our future studies.

In conclusion, a novel AGWLP strategy was developed for morphological reconstruction of FMT. Compared with the traditional methods, it achieved more accurate results in both localization and morphological recovery of fluorescence probe distribution. We believe this method pushed FMT into a new level of chasing higher spatial accuracy, and brought great promise in benefiting the application of FMT for *in vivo* molecular imaging studies of tumor-bearing mouse models.

ACKNOWLEDGMENT

The authors thank Shixin Jiang, Yu An, and Lin Yin for the support of *in vivo* experiments.

REFERENCES

[1] V. Ntziachristos, C. Bremer, and R. Weissleder, "Fluorescence imaging with near-infrared light: New technological advances that enable *in vivo* molecular imaging," *Eur. Radiol.*, vol. 13, pp. 195–208, Jan. 2003.

[2] R. Weissleder, "Scaling down imaging: Molecular mapping of cancer in mice," *Nature Rev. Cancer*, vol. 2, no. 1, pp. 11–18, Jan. 2002.

[3] R. Weissleder, C.-H. Tung, U. Mahmood, and A. Bogdanov, Jr., "*In vivo* imaging of tumors with protease-activated near-infrared fluorescent probes," *Nature Biotechnol.*, vol. 17, pp. 375–378, Apr. 1999.

[4] V. Ntziachristos, J. Ripoll, L. V. Wang, and R. Weissleder, "Looking and listening to light: The evolution of whole-body photonic imaging," *Nature Biotechnol.*, vol. 23, pp. 313–320, Mar. 2005.

[5] A. Ale, V. Ermolayev, E. Herzog, C. Cohrs, M. H. De Angelis, and V. Ntziachristos, "FMT-XCT: *In vivo* animal studies with hybrid fluorescence molecular tomography–X-ray computed tomography," *Nature methods*, vol. 9, pp. 615–620, May 2012.

[6] B. W. Pogue, B. Chen, X. Zhou, and P. J. Hoopes, "Analysis of sampling volume and tissue heterogeneity on the *in vivo* detection of fluorescence," *J. Biomed. Opt.*, vol. 10, Jul. 2005, Art. no. 041206.

[7] R. W. Holt *et al.*, "Tomography of epidermal growth factor receptor binding to fluorescent Affibody *in vivo* studied with magnetic resonance guided fluorescence recovery in varying orthotopic glioma sizes," *J. Biomed. Opt.*, vol. 20, Feb. 2015, Art. no. 026001.

[8] P. Mohajerani and V. Ntziachristos, "An inversion scheme for hybrid fluorescence molecular tomography using a fuzzy inference system," *IEEE Trans. Med. Imag.*, vol. 35, no. 2, pp. 381–390, Feb. 2016.

[9] S. Jiang *et al.*, "Novel $l_{2,1}$-norm optimization method for fluorescence molecular tomography reconstruction," *Biomed. Opt. Express*, vol. 7, no. 6, pp. 2342–2359, Jun. 2016.

[10] J. Shi, F. Liu, J. Zhang, J. Luo, and J. Bai, "Fluorescence molecular tomography reconstruction via discrete cosine transform-based regularization," *J. Biomed. Opt.*, vol. 20, no. 5, May 2015, Art. no. 055004.

[11] E. Edjlali and Y. Bérubé-Lauzière, "L_q–L_p optimization for multigrid fluorescence tomography of small animals using simplified spherical harmonics," *J. Quant. Spectrosc. Radiat. Transf.*, vol. 205, pp. 163–173, Jan. 2018.

[12] D. Zhu and C. Li, "Nonconvex regularizations in fluorescence molecular tomography for sparsity enhancement," *Phys. Med. Biol.*, vol. 59, no. 12, pp. 2901–2912, May 2014.

[13] D. Han *et al.*, "Efficient reconstruction method for L1 regularization in fluorescence molecular tomography," *Appl. Opt.*, vol. 49, no. 36, pp. 6930–6937, Dec. 2010.

[14] S. Zhang *et al.*, "Robust reconstruction of fluorescence molecular tomography based on sparsity adaptive correntropy matching pursuit method for stem cell distribution," *IEEE Trans. Med. Imag.*, vol. 37, no. 10, pp. 2176–2184, Oct. 2018.

[15] X. He, H. Guo, J. Yu, X. Zhang, and Y. Hou, "Effective and robust approach for fluorescence molecular tomography based on CoSaMP and SP_3 model," *J. Innov. Opt. Health Sci.*, vol. 9, no. 6, Nov. 2016, Art. no. 1650024.

[16] A. Behrooz, H.-M. Zhou, A. A. Eftekhar, and A. Adibi, "Total variation regularization for 3D reconstruction in fluorescence tomography: Experimental phantom studies," *Appl. Opt.*, vol. 51, no. 34, pp. 8216–8227, Dec. 2012.

[17] S. M. Hejazi, S. Sarkar, and Z. Darezereshki, "Fast multislice fluorescence molecular tomography using sparsity-inducing regularization," *J. Biomed. Opt.*, vol. 21, no. 2, Feb. 2016, Art. no. 026012.

[18] J. Dutta, S. Ahn, C. Li, S. R. Cherry, and R. M. Leahy, "Joint L^1 and total variation regularization for fluorescence molecular tomography," *Phys. Med. Biol.*, vol. 57, no. 6, p. 1459, Mar. 2012.

[19] X. Cao *et al.*, "An adaptive Tikhonov regularization method for fluorescence molecular tomography," *Med. Biol. Eng. Comput.*, vol. 51, no. 8, pp. 849–858, Aug. 2013.

[20] S. C. Davis, K. S. Samkoe, J. A. O'Hara, S. L. Gibbs-Strauss, K. D. Paulsen, and B. W. Pogue, "Comparing implementations of magnetic-resonance-guided fluorescence molecular tomography for diagnostic classification of brain tumors," *J. Biomed. Opt.*, vol. 15, no. 5, Sep. 2010, Art. no. 051602.

[21] S. C. Davis *et al.*, "Dynamic dual-tracer MRI-guided fluorescence tomography to quantify receptor density *in vivo*," *PNAS*, vol. 110, no. 22, pp. 9025–9030, May 2013.

[22] R. B. Schulz *et al.*, "Hybrid system for simultaneous fluorescence and X-ray computed tomography," *IEEE Trans. Med. Imag.*, vol. 29, no. 2, pp. 465–473, Feb. 2010.

[23] J. T. Elliott *et al.*, "Simultaneous *in vivo* fluorescent markers for perfusion, protoporphyrin metabolism, and EGFR expression for optically guided identification of orthotopic glioma," *Clin. Cancer Res.*, vol. 23, no. 9, pp. 2203–2212, May 2017.

[24] L. Qiu *et al.*, "Gliomas: Motexafin gadolinium-enhanced molecular MR imaging and optical imaging for potential intraoperative delineation of tumor margins," *Radiology*, vol. 279, no. 2, pp. 400–409, Nov. 2015.

[25] M. F. Kircher *et al.*, "A brain tumor molecular imaging strategy using a new triple-modality MRI-photoacoustic-Raman nanoparticle," *Nature Med.*, vol. 18, no. 5, pp. 829–834, Apr. 2012.

[26] K. M. Tichauer *et al.*, "Dual-tracer background subtraction approach for fluorescent molecular tomography," *J. Biomed. Opt.*, vol. 18, no. 1, Jan. 2013, Art. no. 016003.

[27] Y. Gao, K. Wang, S. Jiang, Y. Liu, T. Ai, and J. Tian, "Bioluminescence tomography based on Gaussian weighted Laplace prior regularization for *In Vivo* morphological imaging of glioma," *IEEE Trans. Med. Imag.*, vol. 36, no. 11, pp. 2343–2354, Nov. 2017.

[28] R. Baikejiang, Y. Zhao, B. Z. Fite, K. W. Ferrara, and C. Li, "Anatomical image-guided fluorescence molecular tomography reconstruction using kernel method," *J. Biomed. Opt.*, vol. 22, no. 5, May 2017, Art. no. 055001.

[29] Y. Lv *et al.*, "A multilevel adaptive finite element algorithm for bioluminescence tomography," *Opt. Express*, vol. 14, no. 18, pp. 8211–8223, Sep. 2006.

[30] D. Wang, X. Liu, Y. Chen, and J. Bai, "A novel finite-element-based algorithm for fluorescence molecular tomography of heterogeneous media," *IEEE Trans. Inf. Technol. Biomed.*, vol. 13, no. 5, pp. 766–773, Sep. 2009.

[31] C. Soares, P. B. Brazdil, and P. Kuba, "A meta-learning method to select the kernel width in support vector regression," *Mach. Learn.*, vol. 54, no. 3, pp. 195–209, Mar. 2004. [Online]. Available: https://link.springer.com/article/10.1023/B:MACH.0000015879.28004.9b

[32] R. Fletcher and C. M. Reeves, "Function minimization by conjugate gradients," *Comput. J.*, vol. 7, no. 2, pp. 149–154, Jan. 1964.

[33] K. Wang *et al.*, "Optical molecular imaging frontiers in oncology: The pursuit of accuracy and sensitivity," *Engineering*, vol. 1, no. 3, pp. 309–323, Sep. 2015.

[34] M. Liu *et al.*, "*In vivo* pentamodal tomographic imaging for small animals," *Biomed. Opt. Express*, vol. 8, no. 3, pp. 1356–1371, Mar. 2017.

[35] S. L. Jacques, "Optical properties of biological tissues: A review," *Phys. Med. Biol.*, vol. 58, no. 11, pp. R37–R61, May 2013.

[36] G. Alexandrakis, F. R. Rannou, and A. F. Chatziioannou, "Tomographic bioluminescence imaging by use of a combined optical-PET (OPET) system: A computer simulation feasibility study," *Phys. Med. Biol.*, vol. 50, no. 17, pp. 4225–4241, Aug. 2005.

[37] Y. An *et al.*, "A novel region reconstruction method for fluorescence molecular tomography," *IEEE Trans. Biomed. Eng.*, vol. 62, no. 7, pp. 1818–1826, Jul. 2015.

[38] F. Maes, A. Collignon, D. Vandermeulen, G. Marchal, and P. Suetens, "Multimodality image registration by maximization of mutual information," *IEEE Trans. Med. Imag.*, vol. 16, no. 2, pp. 187–198, Apr. 1997.